LAWRENCE
LIVERMORE
NATIONAL
LABORATORY

UCRL-TR-234487

Pulsed Laser-Based X-Ray Sources for Rapid-Cool DT Layer Characterization

Jeffrey A. Koch, Eduard Dewald, Nobuhiko Izumi, Bernie Kozioziemski, Otto Landen, Craig Siders

September 10, 2007

This work was performed under the auspices of the U.S. Department of Energy by University of California, Lawrence Livermore National Laboratory under Contract W-7405-Eng-48.

August 29, 2007

Pulsed Laser-based X-ray Sources for Rapid-Cool DT Layer Characterization

Jeffrey A. Koch, Eduard Dewald, Nobuhiko Izumi, Bernie Kozioziemski, Otto Landen, Craig Siders

I. Introduction

Ignition targets for the National Ignition Facility (NIF) will contain a cryogenically cooled ~ 75 μm-thick deuterium/tritium (DT) ice layer surrounded by a ~ 150 μm-thick beryllium (Be) shell [1]. Ignition target design optimization depends sensitively on the achievable inner surface quality of the ice layer and on the pressure of the DT gas inside the ice, which is determined by the temperature of the ice. The inner ice layer surface is smoothest at temperatures just below the DT ice/liquid/gas triple point (3T), but current ignition target designs require central gas pressures of 0.3 mg/cm^3, corresponding to an ice layer temperature 1.5 °K below the triple point (3T-1.5). At these lower temperatures, the ice layer quality degrades due to the formation of cracks and other features. [2]

Ongoing experiments suggest that a stable layer at 3T-1.5 cannot be made with a surface quality that meets current requirements. Ignition margin can be recovered by operating with more laser energy in a different target design, but the desire to minimize the required laser energy leads us to explore alternative methods of meeting the ice surface requirements at 3T-1.5. Our current plan is to utilize a rapid-cool strategy, where a stable smooth ice layer is formed near 3T, and the target is then rapidly cooled over second timescales to 3T-1.5. Available data suggest that the timescale for crack formation and layer surface quality degradation is longer than the timescale for central gas pressure reduction, allowing a several-second time window where the target meets both layer quality and central gas pressure requirements. On NIF, we intend to implode the capsule during this short time window.

Since Be shells are opaque to visible light, x-ray radiography is used to characterize the surface quality of DT ice in ignition capsules. DT ice produces negligible absorption contrast at x-ray energies high enough to penetrate the Be shell, so radiography is performed in refraction-enhanced (phase contrast) mode [3,4]. This technique dramatically enhances the contrast of the DT ice/gas interface as well as of cracks in the DT ice, but places challenging requirements upon the source brightness and source size. Continuous-emission laboratory x-ray sources provide high-quality images over ~ minute integration timescales, but this timescale is far too long to characterize the degradation of rapid-cool DT ice layers. We therefore require new sources and/or new imaging geometries in

order to adequately characterize a DT ice layer during rapid-cool and verify that design-based requirements will be met at NIF shot time.

Laser-generated x-ray production has been investigated for many years in connection with inertial confinement fusion research, and a large database exists for thermal (hot plasma) x-ray production efficiencies for various ns- and sub-ns-duration pulsed laser irradiation conditions. In recent years, the development of short-pulse lasers (~ ps-duration or less) has led to the development of non-thermal (relativistic electron-driven) x-ray sources produced by ultra-high-intensity laser pulses, and these sources have some advantages and disadvantages over conventional thermal x-ray sources. Simple estimates suggest that many of these sources might be utilized for flash radiography of rapid-cool DT layers, provided that a suitable match can be found between DT layer imaging requirements and laser source characteristics such as x-ray energy conversion, x-ray photon energy, and x-ray spot size. Other considerations include detector spatial resolution and detection efficiency, damage to the capsule and/or detector due to debris, and the cryogenic environment. The result is a broad region of acceptable parameter space, and laser-produced plasma sources that may fall within this parameter space when suitably optimized.

In this memo, we quantitatively explore the imaging parameter space that might be acceptable for flash radiography of rapid-cool DT layers. We also evaluate laser-produced plasma x-ray sources that might fall within this parameter space, with the goal of developing specific imaging geometries tailored for optimum performance with specific laser sources.

II. Analytical photometrics requirements

Current laboratory characterization uses a Kevex electron-beam x-ray source with a high-magnification radiography geometry [5]. The source diameter is approximately 4 μm, object and detector distances are 75 mm and 685 mm respectively, and the source emits primarily 8 keV x-rays. Estimates based on source emission and detector efficiency indicate that this setup provides images with approximately 4000 detected photons per resolution element, and with an effective signal-to-noise ratio of approximately 30 over a resolution element. The reduction below the photon statistical limit is due in part to filter transmission spatial variations that are typically left uncorrected; a lower bound on acceptable signal-to-noise ratio would then permit as few as ~ 1000 photons per resolution element to be detected if fixed-pattern backgrounds are subtracted. A sketch of the Kevex-based imaging system is shown in Figure 1 below.

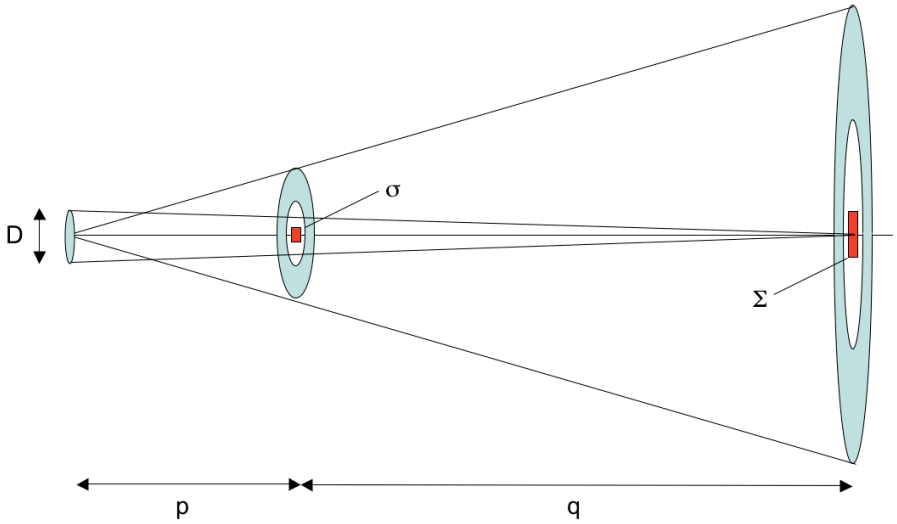

Figure 1: High-magnification radiography with a small source. D is the x-ray source diameter, p is the distance between the source and the object, q is the distance between the object and the detector, σ is the resolution at the object, and Σ is magnified resolution at the detector plane.

Referring to Fig. 1, the object resolution σ is given by:

$$\frac{\sigma}{q} = \frac{D}{p+q} \tag{1}$$

With D = 4 μm, p = 75 mm, and q = 685 mm, σ ≈ 3.6 μm. This object resolution projects to a resolution element in the detector plane given by:

$$\frac{\Sigma}{p+q} = \frac{\sigma}{p} \tag{2}$$

This is Σ = 36.5 μm. The number of detected photons per resolution element, N, is given by:

$$N = I0 * \frac{\pi D^2}{4} * \frac{\pi \Sigma^2 / 4}{4\pi (p+q)^2} * T * \eta \tag{3}$$

where I0 is the source brightness in photons/cm^2/sphere, T is the (energy-dependent) shell and cryostat window transmission in the chosen region of the object, and η is the (energy-dependent) detection efficiency. As noted above, previous experiments indicate N ≈ 4000.

Finally, we need to consider image contrast in refraction-enhanced radiography. Figure 2 below shows the ray paths for imaging the limb of a spherical phase shell, equivalent to observing the ice/gas interface in a DT

layered target. Refraction near the limb, where incident angles approach zero, steers rays towards the center of the projected image, leaving a dark circular band surrounding a bright circle of refracted light. This refractive enhancement of contrast allows the ice/gas interface to be observed even when there is negligible absorption contrast. Similar effects improve the contrast of cracks and other features in the central regions of the projected image, but we concentrate here on limb refraction because it is the primary means for determining layer quality.

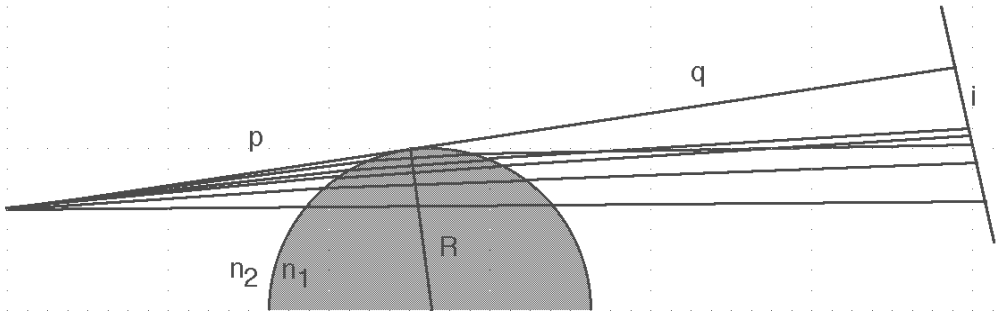

Figure 2: Sketch of ray paths for imaging the limb of a DT layered capsule. p is the source/object distance, q is the object/detector distance, n2 is the refractive index of the ice, n1 > n2 is the refractive index of the central gas, R is the inner ice surface radius, and i is the width of the projected phase-contrast dark band.

Previous analytical work [3] has calculated that the dark band width i is given by:

$$i = 3\left(\frac{p+q}{p}\right)^{1/3}\left(q(n1-n2)\sqrt{R/2}\right)^{2/3} \tag{4}$$

Image contrast relates to the width of the refraction-enhanced band divided by the projected object resolution Σ, so:

$$\frac{i}{\Sigma} = 3\frac{(p+q)^{1/3}p^{2/3}}{Dq^{1/3}}\left((n1-n2)\sqrt{R/2}\right)^{2/3} \tag{5}$$

(n1-n2) is approximately 1.29e-6 at 8 keV for ice and gas densities of 0.25 and 0.0003 g/cm^2, respectively, and scales as inverse photon energy squared, and R is approximately 1 mm, so $i/\Sigma \approx 1.3$.

Given this baseline, we can extrapolate to other imaging geometries and source characteristics and determine if images with comparable contrast, resolution, and signal-to-noise could be obtained in fast flash radiographs. Summarizing, based on the above analysis we desire:

$$\sigma_0 = 3.6\ \mu m$$

$$(i/\Sigma)_0 = 1.3$$
$$N_0 = 4000$$

Where the subscript 0 refers to the baseline (Kevex) quantities. We also implicitly require that the x-ray detector have spatial resolution adequate to resolve the magnified object resolution, typically requiring a detector resolution better than $\Sigma/2$. While these numbers relate to current laboratory image parameters, it is important to note that they are not firm requirements; if degradation of rapid-cool DT layer quality can be quantified with relaxed parameters, then those relaxed parameters would be acceptable. In particular, as indicated above, as few as N=1000 detected photons per resolution element would be acceptable if fixed-pattern backgrounds can be subtracted. Additionally, somewhat reduced (~ 2x) spatial resolution σ is probably acceptable, particularly if refraction contrast (i/Σ) is increased.

We consider two different flash radiography geometries, pinhole-restricted high magnification and full-source low- or high-magnification, as illustrated in Fig. 3 below.

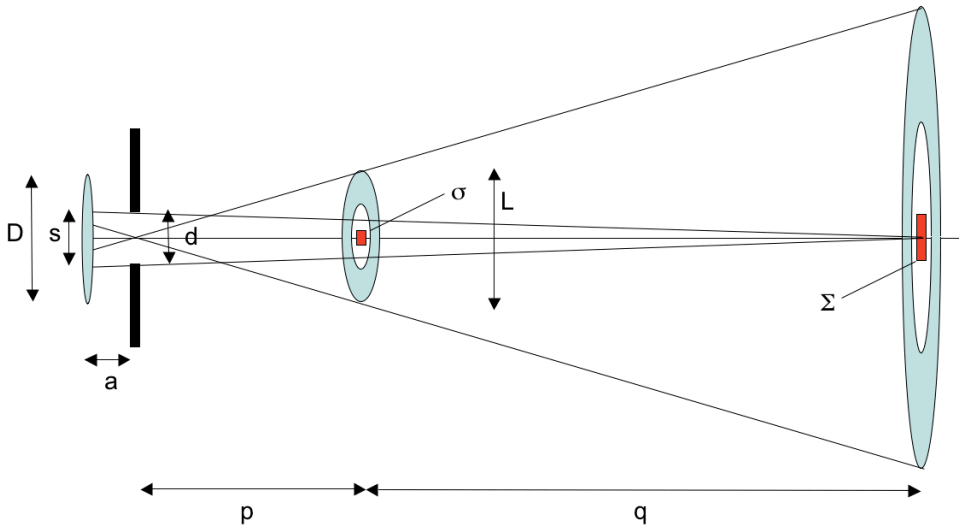

Figure 3(a): Pinhole restricted radiography with a backlit pinhole source. D is the x-ray source diameter, s is the pinhole-restricted source diameter, d is the pinhole diameter, a is the distance between the pinhole and the source, p is the distance between the pinhole and the object, q is the distance between the object and the detector, L is the object diameter, σ is the resolution at the object, and Σ is the magnified resolution at the detector plane.

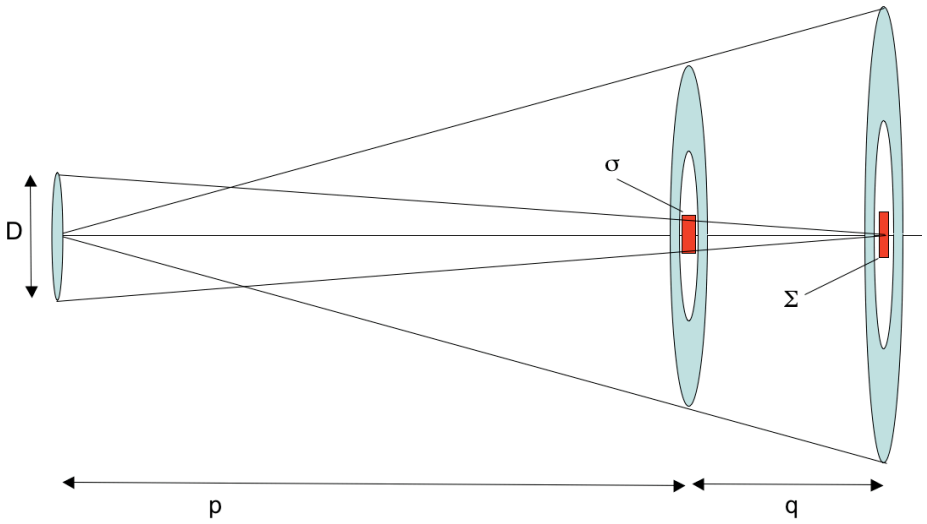

Figure 3(b): Full-source radiography. D is the x-ray source diameter, p is the distance between the source and the object, q is the distance between the object and the detector, σ is the resolution at the object, and Σ is magnified resolution at the detector plane. The sketch illustrates a low-magnification geometry, but high magnification could be used as well if the source size is small enough, as shown in Fig. 1.

In Fig. 3(a), we assume that the x-ray source is too large to provide the required object spatial resolution, and must be restricted with a pinhole. In Fig. 3(b), we assume that the full x-ray source size is utilized. In the latter case, either low- or high-magnification radiography geometries could be used. For low-magnification radiography, the magnification must be reduced to M < 2 in order to achieve the required object resolution, and a high-resolution detector must be utilized; in high-magnification radiography, as with the Kevex source, the source size must be reduced to less than twice the desired object resolution in order to achieve that object resolution. We now explore the requirements for both types of geometries to achieve imaging parameters comparable to those achieved with the Kevex laboratory source.

(A): High-magnification backlit pinhole imaging

In high-magnification backlit pinhole imaging, the object resolution is determined by the pinhole diameter. We require:

$$d = \frac{p+q}{q}\sigma = \frac{(3.6\mu m)(p+q)}{q}\left(\frac{\sigma}{3.6\mu m}\right) \tag{6}$$

The backlit pinhole geometry reduces the area of the source that is used for radiography, and also places constraints on the distance between the pinhole and

source in order to allow the full object to be imaged without vignetting. We can see from the geometry above that full-field imaging requires:

$$\frac{D}{a} = \frac{L}{p}, \quad a = \frac{Dp}{L} \tag{7}$$

where L here is nominally 2 mm. The actual area of the source used for imaging, s, is given by:

$$s = \frac{(p+q+a)d}{(p+q)} \tag{8}$$

The ratio i/Σ is given by:

$$\begin{aligned} \frac{i}{\Sigma} &= 3\frac{(p+q)^{1/3}p^{2/3}}{dq^{1/3}}\left((n1-n2)\sqrt{R/2}\right)^{2/3} \\ &= \frac{3p^{2/3}q^{2/3}}{(p+q)^{2/3}(3.6\mu m)}\left(\frac{3.6\mu m}{\sigma}\right)\left((n1-n2)\sqrt{R/2}\right)^{2/3} \end{aligned} \tag{9}$$

This would be equated with $(i/\Sigma)_0 = 1.3$ in order to match the Kevex numbers above, which in turn places constraints on the relationship between p and q:

$$\frac{3p^{2/3}q^{2/3}}{(p+q)^{2/3}(3.6\mu m)}\left(\frac{3.6\mu m}{\sigma}\right)\left((n1-n2)\sqrt{R/2}\right)^{2/3} = 1.3\left(\frac{(i/\Sigma)}{1.3}\right) \tag{10}$$

If we explicitly include the energy scaling of (n1-n2) and set R = 1 mm, we obtain:

$$\frac{p^{2/3}q^{2/3}}{(p+q)^{2/3}} = 1.03E_{keV}^{4/3}\left(\frac{\sigma}{3.6\mu m}\right)\left(\frac{(i/\Sigma)}{1.3}\right) \tag{11}$$

where p and q are in mm. We can combine this with eq. (6) to write a constraint on p alone:

$$p = 0.29E_{keV}^2 d\left(\frac{\sigma}{3.6\mu m}\right)^{1/2}\left(\frac{(i/\Sigma)}{1.3}\right)^{3/2} \tag{12}$$

where p is in mm and d is in μm. Finally, we can calculate the number of detected photons per resolution element as:

$$N = I0 * \frac{\pi s^2}{4} * \frac{\pi\Sigma^2/4}{4\pi(p+q+a)^2} * T * \eta \tag{13}$$

$$\approx I0 * \frac{\pi}{64} * \frac{(p+q)^2 (3.6\mu m)^4}{p^2 q^2} \left(\frac{\sigma}{3.6\mu m} \right)^4 * T * \eta$$

where we neglect a as small compared with p+q. Since we desire N = 4000, this places a constraint on I0, which we write as:

$$I0 > 4.85e16 \frac{p^2 q^2}{(p+q)^2 T_E \eta_E} \left(\frac{3.6\mu m}{\sigma} \right)^4 \left(\frac{N}{4000} \right) \tag{14}$$

where we explicitly note that T and η are functions of photon energy E. This takes a simple form if we include the constraint from eq. (11):

$$I0 > 5.37e16 \frac{E_{keV}^4}{T_E \eta_E} \left(\frac{N}{4000} \right) \left(\frac{3.6\mu m}{\sigma} \right) \left(\frac{(i/\Sigma)}{1.3} \right)^3 \tag{15}$$

The total required x-ray energy, E0, is I0 integrated over the full source diameter D, multiplied by a photon energy conversion factor that adds another multiple of E.

$$E0 > 6.75e-8 \frac{E_{keV}^5 D^2}{T_E \eta_E} \left(\frac{N}{4000} \right) \left(\frac{3.6\mu m}{\sigma} \right) \left(\frac{(i/\Sigma)}{1.3} \right)^3 \tag{16}$$

This energy conversion efficiency implicitly assumes isotropic emission; directional emission (beaming) would reduce the required total energy conversion efficiency. Summarizing and rearranging, a backlit pinhole x-ray source can be used for flash phase-contrast radiography of a DT layered shell with resolution, contrast and signal-to-noise comparable to current laboratory data if the following constraints are met:

Pinhole/object distance (in mm, d and σ in μm and E in keV):

$$p = 0.29 E_{keV}^2 d \left(\frac{\sigma}{3.6\mu m} \right)^{1/2} \left(\frac{(i/\Sigma)}{1.3} \right)^{3/2} \tag{17}$$

Object/detector distance (in mm, d and σ in μm and E in keV):

$$q = \frac{0.29 E_{keV}^2 d}{\left(\frac{d}{\sigma} - 1 \right)} \left(\frac{\sigma}{3.6\mu m} \right)^{1/2} \left(\frac{(i/\Sigma)}{1.3} \right)^{3/2} \tag{18}$$

Pinhole/source distance (in mm, D and p in mm):

$$a = \frac{Dp}{L} \tag{19}$$

Source brightness (in photons/cm²/sphere, E in keV):

$$I0 > 5.37e16 \frac{E_{keV}^4}{T_E \eta_E} \left(\frac{N}{4000} \right) \left(\frac{3.6\mu m}{\sigma} \right) \left(\frac{(i/\Sigma)}{1.3} \right)^3 \tag{20}$$

Source x-ray energy output (in joules/sphere, E in keV, D in μm):

$$E0 > 6.75e-8 \frac{E_{keV}^5 D^2}{T_E \eta_E} \left(\frac{N}{4000} \right) \left(\frac{3.6\mu m}{\sigma} \right) \left(\frac{(i/\Sigma)}{1.3} \right)^3 \tag{21}$$

Finally, the detector resolution must typically be better than Σ/2, which is (p+q)σ/2p.

(B): Full-source imaging

The above analysis also applies directly to full-source imaging, except that constraints on the pinhole diameter now apply to the entire source diameter. We simply set a equal to zero, and replace d with D. The constraints become:

Pinhole/object distance (in mm, D and σ in μm and E in keV):

$$p = 0.29 E_{keV}^2 D \left(\frac{\sigma}{3.6\mu m} \right)^{1/2} \left(\frac{(i/\Sigma)}{1.3} \right)^{3/2} \tag{22}$$

Object/detector distance (in mm, D and σ in μm and E in keV):

$$q = \frac{0.29 E_{keV}^2 D}{\left(\frac{D}{\sigma} - 1 \right)} \left(\frac{\sigma}{3.6\mu m} \right)^{1/2} \left(\frac{(i/\Sigma)}{1.3} \right)^{3/2} \tag{23}$$

Source brightness (in photons/cm²/sphere, E in keV):

$$I0 > 5.37e16 \frac{E_{keV}^4}{T_E \eta_E} \left(\frac{N}{4000} \right) \left(\frac{3.6\mu m}{\sigma} \right) \left(\frac{(i/\Sigma)}{1.3} \right)^3 \tag{24}$$

Source x-ray energy output (in joules/sphere, E in keV, D in μm):

$$E0 > 6.75e-8\frac{E_{keV}^5 D^2}{T_E \eta_E}\left(\frac{N}{4000}\right)\left(\frac{3.6\mu m}{\sigma}\right)\left(\frac{(i/\Sigma)}{1.3}\right)^3 \quad (25)$$

Again, the detector resolution must typically be better than $(p+q)\sigma/2p$.

For the present purposes, we can assume that the capsule and cryostat windows are made of Be. In this case, we can write functional forms for the transmission T in terms of the total Be thickness and photon energy. Using tabulated x-ray attenuation coefficient data [6], we can write the transmission factor as:

$$T_E = \exp\left(\frac{-t}{8.7689 E_{keV}^{3.0753}}\right) \quad (26)$$

where t is the Be thickness in μm.

In the embedded worksheet Table 1 below (accessible in the Word version of this memo), we tabulate the analytical requirements for various parameters in the backlit pinhole and full-source geometries.

(I/Σ) = 1.3 nominal Kevex = 1.3

σ = 3.6 nominal Kevex = 3.6

N = 4000 nominal Kevex = 4000

Source Diameter D (microns)	Photon energy E (keV)	Pinhole diameter d (microns)	p (mm)	q (mm)
4	2		4.6	41.8
5	2		5.8	14.9
10	2		11.6	6.5
25	2		29.0	4.9
50	2		58.0	4.5

Table 1: Tabulation of various imaging and source parameters for a variety of source diameters and x-ray energies.

Figure 4 below plots some of the results, for low-magnification full-source imaging and 4-μm pinhole restricted high-magnification imaging with 25 μm and 100 μm source diameters.

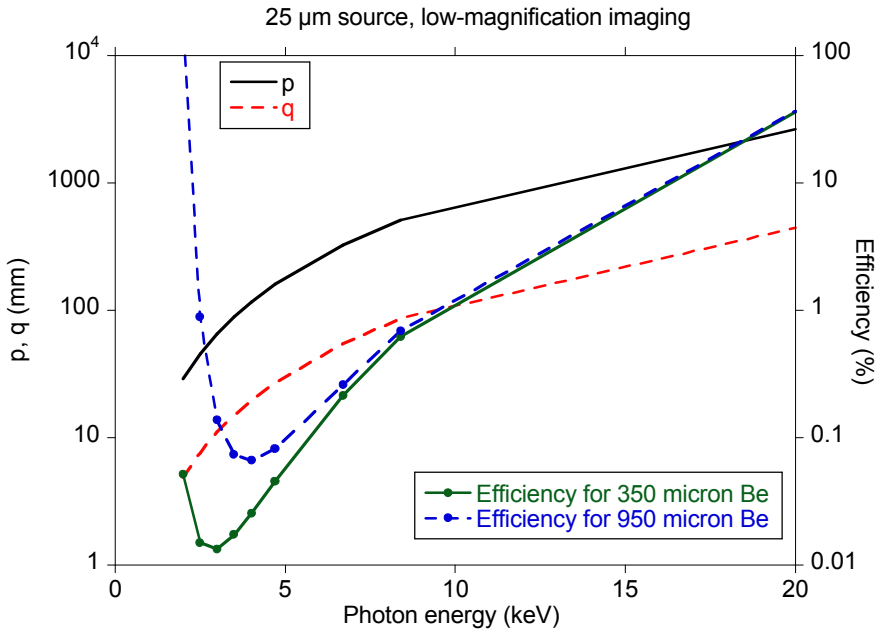

Figure 4(a): Required full-source imaging parameters to match Kevex resolution, contrast, and signal-to-noise, with a 25 µm source and low magnification. Required efficiencies assume a 600-J laser and 50% detection efficiency.

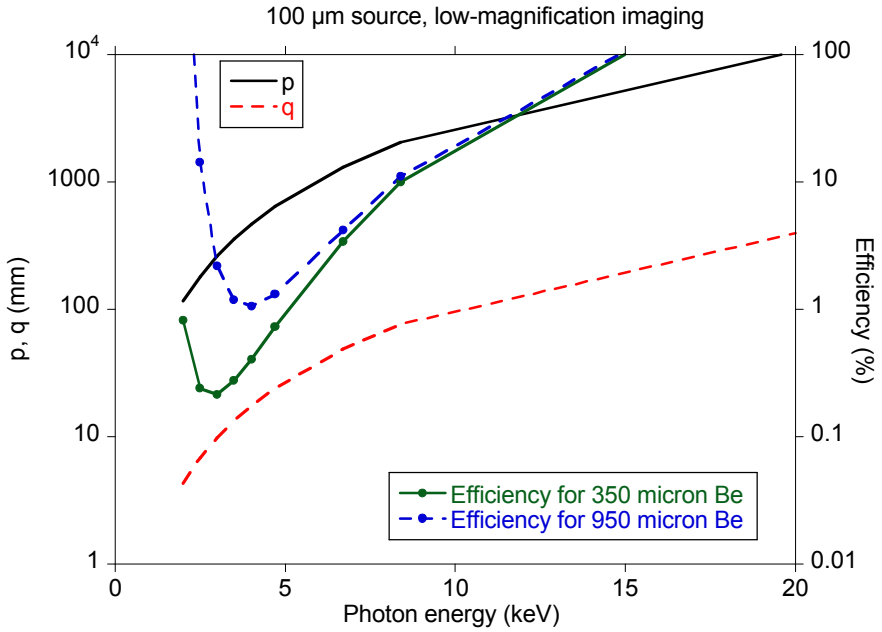

Figure 4(b): Required full-source imaging parameters to match Kevex resolution, contrast, and signal-to-noise, with a 100 µm source and low magnification. Required efficiencies assume a 600-J laser and 50% detection efficiency.

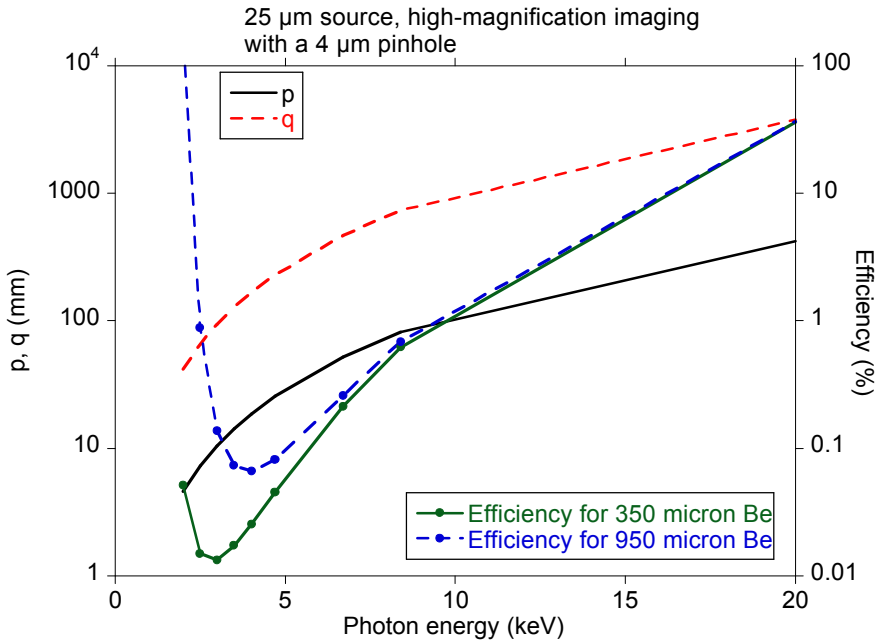

Figure 4(c): Required pinhole-restricted high-magnification imaging parameters to match Kevex resolution, contrast, and signal-to-noise, with a 25 µm source and a 4 µm pinhole. Required efficiencies assume a 600-J laser and 50% detection efficiency.

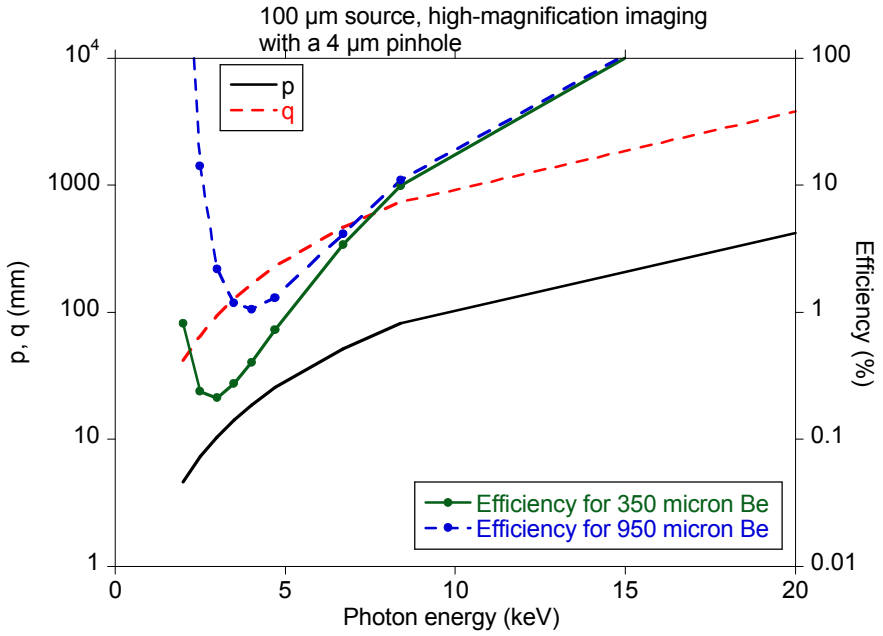

Figure 4(d): Required pinhole-restricted high-magnification imaging parameters to match Kevex resolution, contrast, and signal-to-noise, with a 100 µm source and a 4 µm pinhole. Required efficiencies assume a 600-J laser and 50% detection efficiency.

We find that in general, there is an optimum operating x-ray energy that depends on the total thickness of Be in the shell and cryostat windows, and that

this optimum energy is in the ~ 2-5 keV region for realistic absorption distances. The minimum amount of Be is likely to be around 350 μm, since even for a 40 μm-thick shell the chord length through the shell near the ice/gas interface is ~ 250 μm; a NIF-spec shell with thicker Be windows might amount to ~ 950 μm. This optimum results because the required source energy decreases rapidly (E^5) with decreasing x-ray energy to the point where absorption losses dominate, and the required source energy increases again with decreasing photon energy.

We also find that in many optimal full-source geometries with a large source diameter (low-magnification imaging), the detector distance required to match the Kevex parameters is challengingly small given realistic constraints on placement in a cryogenic environment. We can move the detector back by increasing the photon energy above optimum, or by increasing the effective contrast (i/Σ) above 1.3. These changes have a penalty of requiring higher x-ray conversion efficiency, which can be mitigated somewhat by relaxing the required number of detected photons per resolution element or by increasing the desired source resolution σ above 3.6 μm. Similar considerations apply to pinhole-restricted imaging, where realistic constraints apply to the minimum acceptable distance between the source and the capsule. We explore these tradeoffs more carefully in Section IV.

Finally, we find that smaller source diameters provide significant benefits in required source x-ray energy conversion efficiency, by allowing more x-rays through a pinhole in the backlit-pinhole geometry or by reducing the required source/object distance in the full-source low-magnification geometry. The most efficient geometry would use a ~ 4 μm-diameter source for high-magnification imaging, as is done with the current Kevex source; such a source would only need to emit a few mJ of x-ray energy in order to provide high-quality radiographs using an optimized geometry.

III. Laser-based source characteristics

In this section, we review archival data on x-ray source characteristics in order to evaluate what imaging parameters would be required in order to obtain useful radiograph data of DT ice in cryo-layered capsules using available laser-based x-ray sources.

(A) Long-pulse (thermal x-rays)

Thermal x-ray emission primarily results when lasers of ~ hundreds of ps to ns duration irradiate matter. In this regime, laser energy is absorbed via inverse bremsstrahlung in the low-density ablation plasma, and is transferred to higher-density matter through electron and ion collisions. Some of this energy is re-radiated by the resulting hot plasma, and for typical multi-keV electron temperatures this x-ray emission has multi-keV photon energies. Typical spectra include characteristic K, L or M-shell lines superimposed on a smooth

bremsstrahlung continuum with a slope related to the thermal electron temperature, and conversion efficiencies into characteristic lines or bands of lines are determined by the laser intensity, laser pulse duration, and laser wavelength.

A large body of experimental conversion efficiency data exists for thermal x-rays produced by ~ ns-duration lasers. Matthews *et al.* [7] measured absolute conversion efficiencies for several K- and M-shell emitters including Ti, Ni, Zn, and Au. Some of their results are shown below.

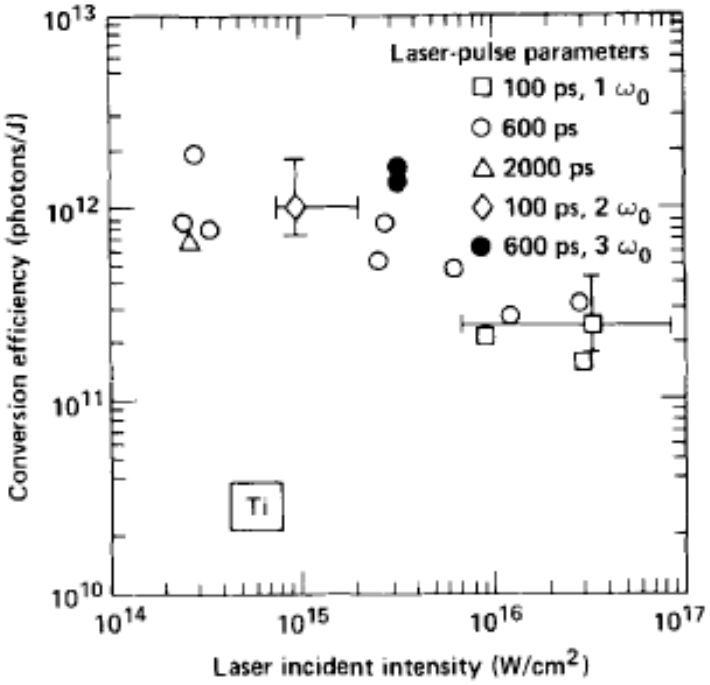

FIG. 2. Line-conversion efficiency as a function of laser intensity for Ti.

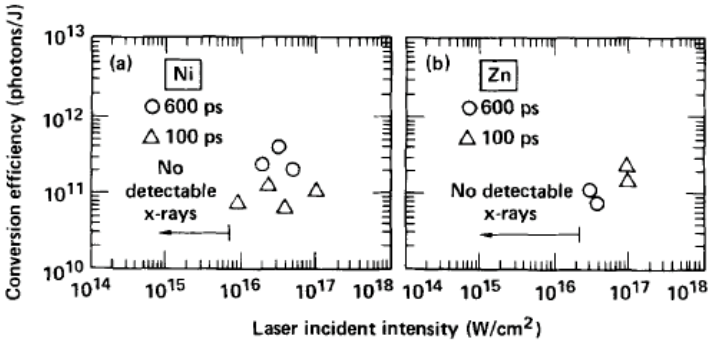

FIG. 3. Line-conversion efficiencies for Ni (7.6 keV) and Zn (8.6 keV).

TABLE III. Comparison[a] of Au *M*-band (1.8–3.6 keV) radiation as a function of laser wavelength and intensity with $\tau_L = 700$ ps.

I_L ($\times 10^{15}$ W/cm^2)	λ_L (microns)	E_L (J)	θ_t^b (degrees)	ξ_s (photons/ laser joule) $\times 10^{14}$
3.0	1.06	600	45	0.05
0.3	1.06	32	12	0.04
~0.3	0.53	25.7	8	0.94
0.3	0.53	24.0	8	0.80
0.2	0.53	21.2	30	0.94
0.2	0.53	22.1	30	1.00
2.0	0.53	35.5	30	0.82
1.0	0.53	37.0	8	0.67
1.0	0.53	38.8	15	0.67
~0.3	0.35	29.2	30	0.23
0.3	0.35	31.1	30	0.43
2.0	0.35	35.9	30	0.87
2.0	0.35	33.1	30	0.97
2.0	0.35	36.5	12	1.30
2.0	0.35	38.5	12	1.30
0.3	0.35	26.7	12	0.39

[a] Tabulated values correspond to different laser shots and may have redundant intensity (I_L) values.
[b] θ_t is the target surface orientation relative to the incident laser beam.

Typical conversion efficiencies for Ti (4.7 keV) are 1e12 photons/joule, or 7.5e-4 J/J, or 0.075% in energy. Ni (7.6 keV) and Zn (8.6 keV) conversion efficiencies are approximately 0.01%, and significant conversion requires laser intensities well in excess of 1e16 W/cm^2. Finally, Au M-band (~ 2.5 keV) conversion efficiencies range from 0.16% to 5%, with significantly higher conversion observed for 2nd and 3rd-harmonic light at intensities in excess of 1e15 W/cm^2. X-ray spot sizes were comparable to the laser spot diameter, and for these data were ~ 500 μm.

Ruggles *et al.* [8] measured absolute conversion efficiencies for several K-shell line emitters using 2nd-harmonic (527 nm) laser irradiation of solid targets at 3-5e15 W/cm^2. Some of their results are shown below.

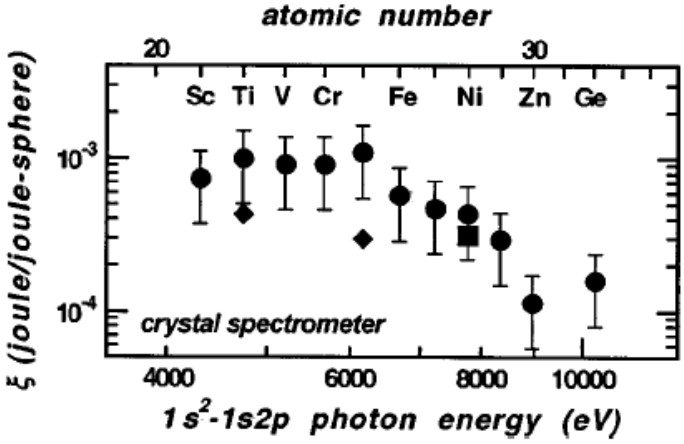

FIG. 5. Conversion efficiency (circles) measured with the convex crystal spectrometer for the He-like $1s^2-1s2p,s$ group of lines compared to Phillion *et al.* for 550 ps (square) and 125 ps (diamonds) laser pulses.

Typical conversion efficiencies ranged from ~ 0.1% for Ti (4.7 keV) to ~ 0.01% for Zn (9 keV). X-ray spot sizes were again comparable to the laser spot diameter, and for these data were ~ 200 μm.

Phillion *et al.* [9] measured absolute conversion efficiencies for Au M-band radiation using 3rd-harmonic (351 nm) laser irradiation of solid Au at various intensities. Their results are reproduced below.

TABLE I. Summary of the fluorescence experiments.

Shot number and target ID	Intensity and energy	Assumed angular distribution	2.472–3.5 keV: Fluorescence measurements (%)	2.472–3.5 keV: Entire spectrum measurements (%)	2.0–3.5 keV: Entire spectrum measurements (%)
17103004	4.9×10^{14} W/cm^2	Lambertian	3.7	4.2[a]	6.9
AUMSKA-01	3100 J	Isotropic	4.2	8.3	13.4
17110309	2.3×10^{14} W/cm^2	Lambertian	4.8	3.3[b]	5.3
AUMSKA-02	1465 J	Isotropic	5.5	6.6	10.3
17110313	1.0×10^{15} W/cm^2	Lambertian	3.9	3.7[a]	5.9
AUMSKA-03	3350 J	Isotropic	4.4	7.3	11.6

[a] $a = 0.32$, $b = 2.3$, $ab = 0.736$. This set of a and b coefficients gives 24% higher fluxes than the set below at small density.
[b] $a = 0.28$, $b = 3.25$, $ab = 0.91$.

Typical conversion efficiencies here were 5-10% depending on laser parameters and assumptions about the emission angular distribution.

Workman *et al.* [10] measured absolute conversion efficiencies for K-shell line emitters using 3rd-harmonic (350 nm) laser irradiation at various intensities. Their results are reproduced below.

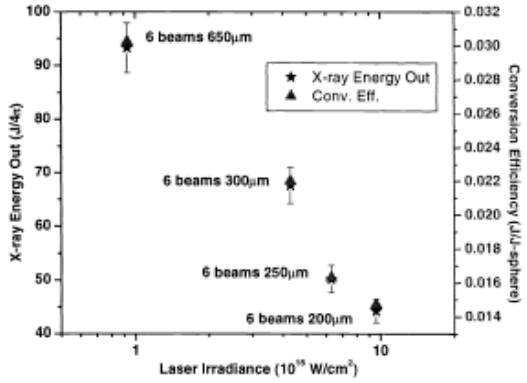

Figure 2: *Scaling of Cr emission and conversion efficiency with laser irradiance. 3 kJ of laser energy were used for each data point while the spot size was changed.*

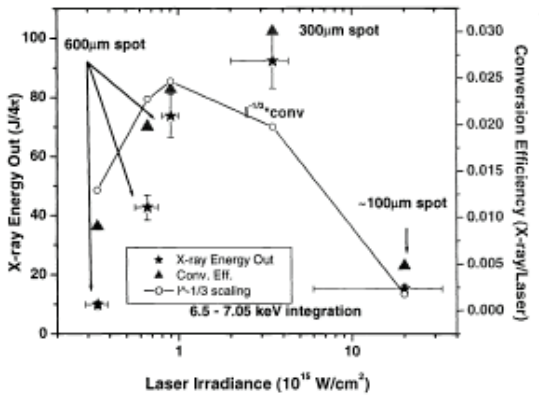

Figure 3: *X-ray yield scaling and conversion efficiency from Fe targets as a function of laser irradiance. The left vertical axis is the energy generated at the source into 4π steradians without correction for crystal reflectivity. The right vertical axis is the conversion of laser energy into x-ray energy. The additional curve is a power law for the irradiance, $I^{-1/3}$, which is typically used for conversion efficiency.*

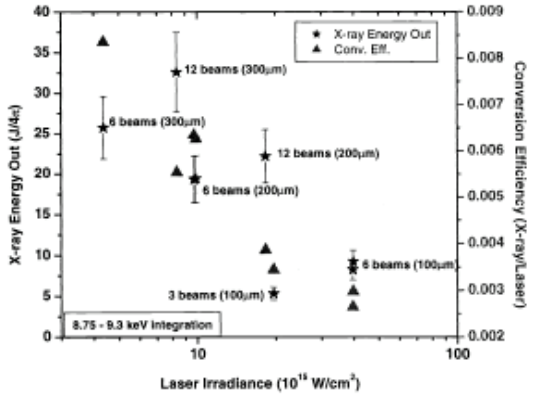

Figure 4: *Scaling of Zn yield and conversion efficiency with laser irradiance. Various combinations of energy and spot sizes were used.*

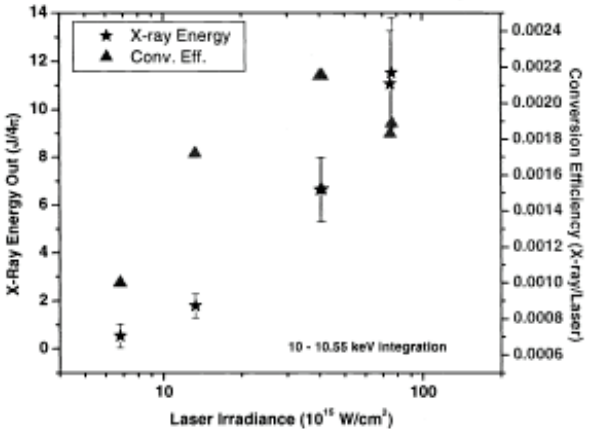

Figure 5: *Scaling of Ge emission and conversion efficiency at 10.3 keV as a function of laser irradiance. All shots were taken at best focus (~100μm) using one, two, six and 12 beams respectively. At 6 and 12 beams there are duplicate data sets.*

Their data show peak conversion efficiencies of 3% for Cr (5.7 keV), 3% for Fe (6.7 keV), 0.8% for Zn (9 keV), and 0.2% for Ge (10.2 keV). These numbers are a

factor of ~ 10 larger than other data suggest, and therefore might be taken as an upper bound for the conversion efficiency that might be expected for K-shell line emitters.

Dewald *et al.* [11] measured Au M-band conversion efficiencies as high as ~ 15% for 351-nm laser intensities of 1e15 W/cm^2. This is higher than numbers reported above by Phillion *et al.*, and therefore might be taken as an upper bound for the conversion efficiency that might be expected for Au M-band sources.

(B) Short-pulse (non-thermal x-rays)

Non-thermal x-ray emission primarily results when lasers of ~ tens of ps or less duration irradiate matter with intensities sufficient to excite non-thermal absorption mechanisms which accelerate electrons to hundreds of keV to MeV energies. These hot electrons produce bremsstrahlung continuum x-ray emission as they slow, and excite K-shell fluorescence in mid- or high-Z target atoms. This process can efficiently produce high-energy x-rays because relatively little of the laser energy is used to heat the target material, and because the x-ray emission spectrum relates to the non-thermal electron energy distribution instead of the thermal distribution.

Park *et al.* [12] published a compilation of Kα conversion efficiency numbers from a variety of experiments irradiating solid foil targets, and we reproduce the results here.

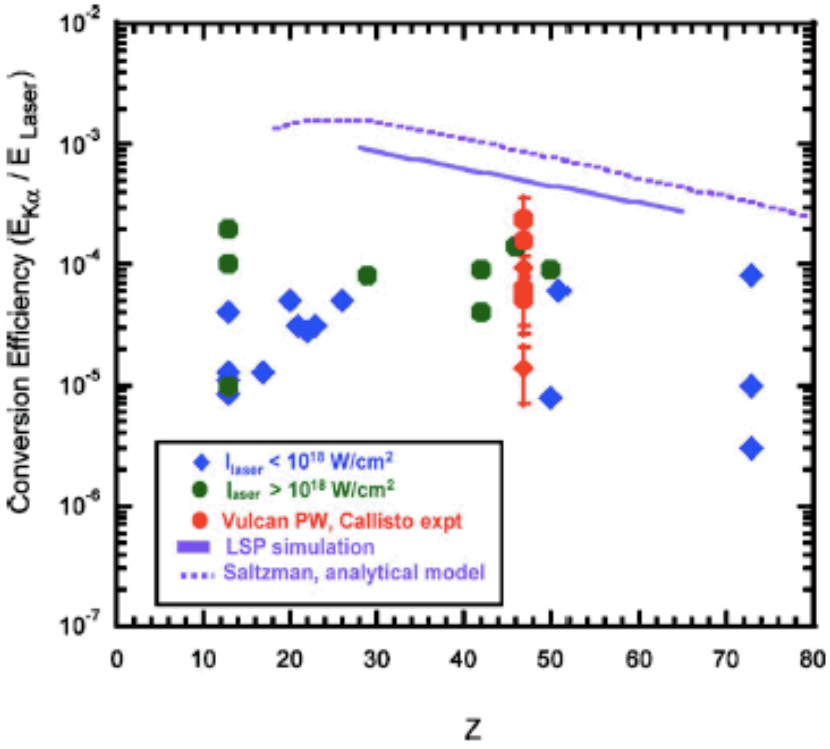

FIG. 5. (Color online) $K\alpha$ conversion efficiency as function of target Z including other experiments (see the text). The diamond plotting symbols correspond to data with $I_L < 10^{18}$ W/cm^2 and the circles to $I_L > 10^{18}$ W/cm^2. The solid line represents the prediction from the LSP modeling and the dotted line is analytical model prediction from Saltzmann.

They found typical conversion efficiencies in the range of 0.001 - 0.01%. This result is essentially independent of target material for Kα x-ray energies ranging from Mg (1.2 keV) to Ta (57 keV). X-ray spot diameters for Park's experiments at 22 keV were observed to be ~ 60 μm, 5-10 times larger than the best-focus laser spot diameter; this is attributed to spreading of relativistic electrons away from the laser focal spot region.

Park's paper also describes experiments with various 2D restricted sources, using 10-20 μm-diameter Cu wires embedded in substrates or excited through a high-Z cone. Data from these experiments are shown below.

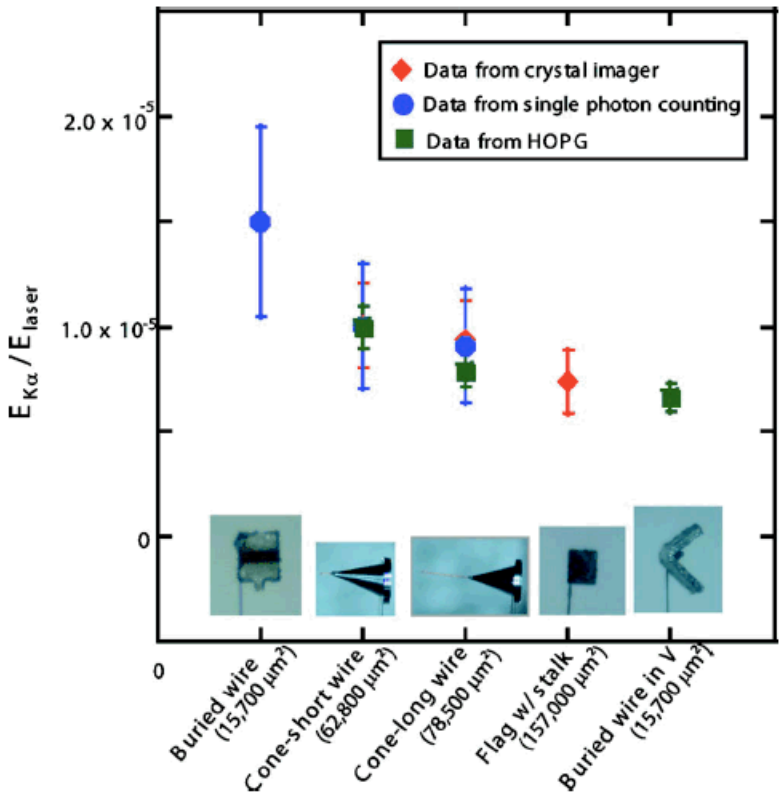

FIG. 12. (Color online) $K\alpha$ yields of microvolume targets with various substrate geometries. We measure the absolute conversion efficiency of these targets to be $\sim 10^{-5}$.

They found the conversion efficiencies for such targets ranged from 0.0006 to 0.0015 %.

IV. Discussion of Promising Options

Experimental data from long-pulse-generated thermal plasmas show conversion efficiencies on the order of 0.01 - 0.1% for helium-like resonance lines below 10 keV, with higher conversion efficiency observed for lower x-ray energies. The data of Workman [10] show conversion efficiencies ~ 10x higher than these values, and might be considered an upper bound for an optimized source. Au M-band emission in the 2-3 keV range can provide much higher conversion efficiency, exceeding ~ 10%, but with a broader emission bandwidth. X-ray emission regions are comparable in size to the laser focal spot diameters, typically ~ 100 μm or more. Experimental data on x-ray conversion efficiency from short-pulse-generated non-thermal plasmas show conversion efficiencies on the order of 0.001 - 0.01% for Kα lines, for x-ray energies up to at least 60 keV. X-ray emission regions are much larger than the (small) laser focal spot diameters, and are ~ 60 μm even for sub-10-μm focal spots. Smaller sources can be obtained through the use of embedded wire or cone-focus wire targets; data

suggests conversion efficiencies of ~ 0.001% can be obtained for ~ 10 μm source diameters.

These data, together with the above analysis of phase contrast imaging requirements, suggest that long-pulse lasers producing relatively low-energy x-rays (2 - 5 keV) are probably optimal for radiographing DT layers in cryogenic capsules. Higher-energy x-rays suffer less absorption through the capsule and cryostat windows, but are not optimal for the present application because they do not refract as much at the ice/gas interface, necessitating larger distances in order to achieve significant contrast. However, since the required x-ray conversion efficiency scales strongly with source size, schemes to reduce the source size with short-pulse-produced plasmas might offset the conversion efficiency disadvantage of working at higher x-ray energies.

In order to evaluate realistic prospects for radiography of rapid-cool layers, we now compare radiography requirements against measured or estimated source characteristics at several facilities.

1) Janus, at the LLNL Jupiter Laser Facility

Experiments were recently performed at the Janus laser facility. These experiments measured front-surface x-ray conversion efficiency and x-ray spot size for a variety of targets, using a single ~ 300 J 527-nm 5-ns-duration beam to irradiate solid foils. Two promising options identified were Au M-band with a conversion efficiency of 1.7% at ~ 2.5 keV, and Ti He-α with a conversion efficiency of 0.37% at 4.7 keV [13]. The measured Ti He-α conversion efficiency is comparable to the archival data shown in Section III (with the exception of Workman *et al.*, as noted above); the measured Au M-band conversion efficiency is comparable to that measured by Matthews *et al.* (2.7%) using 527-nm laser irradiation at a comparable intensity. Source diameters in both cases were approximately 100 μm as measured by an x-ray pinhole camera.

Assuming two 300-J beams and a detector with 50% efficiency, we can compare these numbers against the requirements identified in Section II. The results are shown in Figure 5 below for a low-magnification geometry.

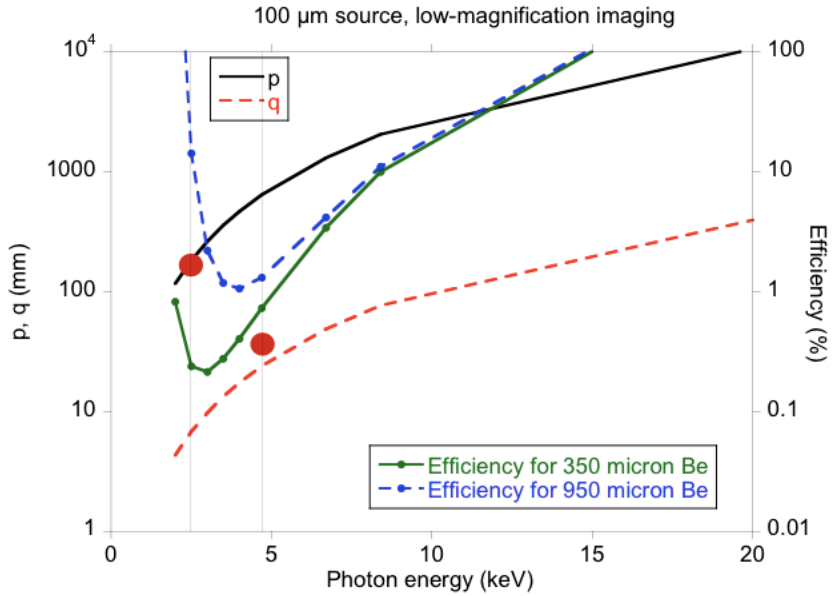

Figure 5: Required full-source imaging parameters to match Kevex resolution, contrast, and signal-to-noise, with a 100 µm source and low magnification. Required efficiencies assume a 600-J laser and 50% detection efficiency. Also plotted are experimental data from Janus.

We see that Au M-band emission from the Janus experiments is more than bright enough to provide low-magnification radiographs comparable to current Kevex laboratory data, provided the total thickness of Be is minimized. Uranium M-band was not measured in these experiments, but assuming comparable conversion at ~ 4 keV it is likely that this source would be sufficient even for full-thickness Be shells and relatively thick Be cryostat windows. We also see that Ti He-α conversion efficiency is not quite high enough to match the current Kevex data quality.

The main issue with using Au M-band emission for this application is the necessity of placing the detector very close to the object; for the optimized case above, this distance would be ~ 10 mm. This is probably possible, but it would require cryostat hardware modifications; it would be desirable to move the detector back to at least 25 mm. Two variations could accomplish this, by increasing i/Σ by a factor of two and possibly by relaxing the resolution requirement from 3.6 µm to 5 µm. These are shown below.

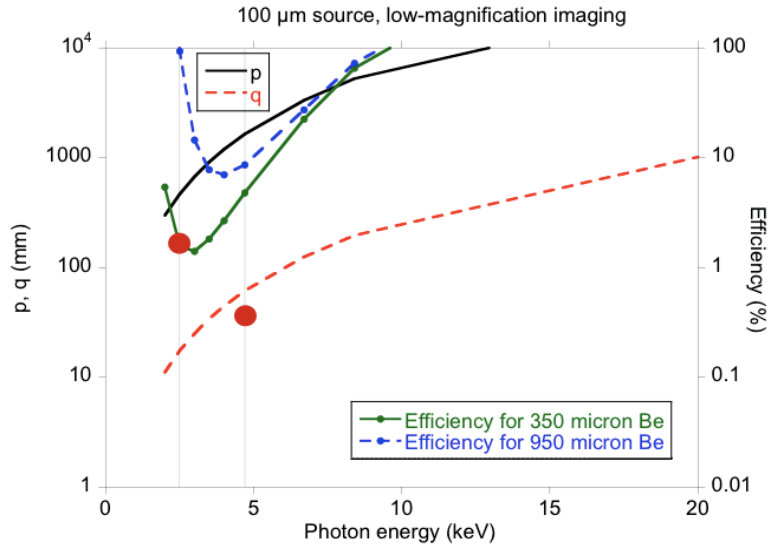

Figure 6: Requirements and Janus data points from Fig. 5, replotted assuming a dark band width twice as large as current Kevex data.

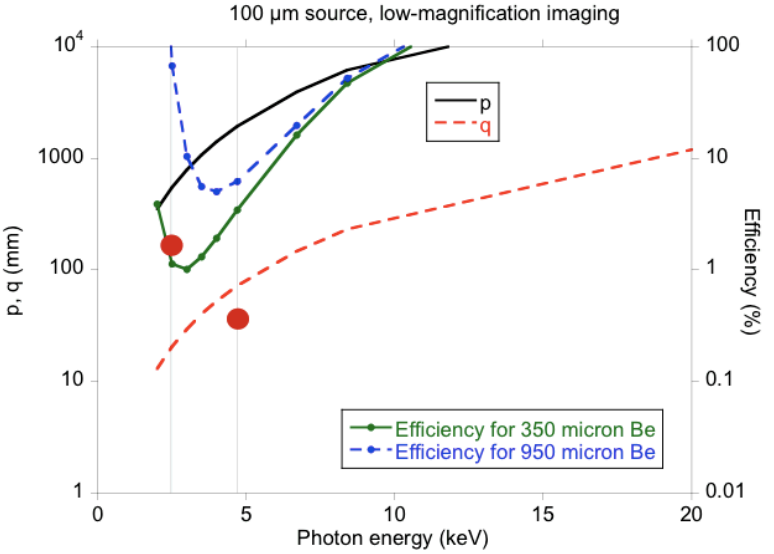

Figure 7: Requirements and Janus data points from Fig. 5, replotted assuming a dark band width twice as large as current Kevex data and a resolution of 5 μm instead of 3.6 μm.

The detector distance in Fig. 6 is ~ 25 mm, and in Fig. 7 it is ~ 42 mm. Either option would probably provide adequate radiograph quality.

It is worth noting that a significant improvement in image brightness could be obtained if the source size could be reduced. Figure 8 below replots the Janus data results assuming the same conversion efficiency could be obtained for a 25 μm source (based on the literature data shown in Section III, it could in fact be higher at the associated higher laser intensities). In this case, either Au M-band or Ti He-α could be used even with full-thickness shells to provide radiographs with signal-to-noise superior to current Kevex laboratory data.

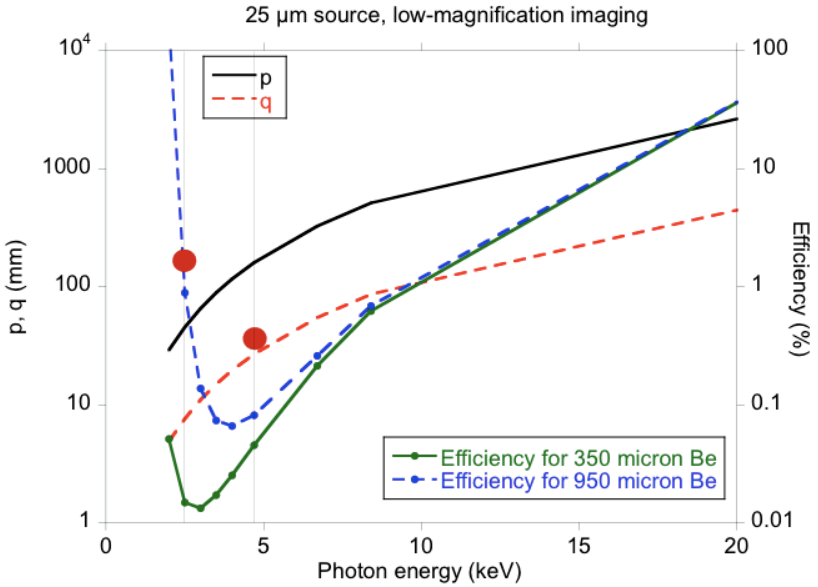

Figure 8: Requirements and Janus data points from Fig. 5, replotted assuming a 25 µm source diameter instead of 100 µm.

2) Titan, at the LLNL Jupiter Laser Facility

The Titan short-pulse laser facility can optimistically provide ~ 0.01% conversion efficiency from a 60 µm x-ray source, or 0.001% conversion efficiency from a 10 µm x-ray source. Below we plot these expected numbers against requirements assuming 8 keV and 22 keV x-ray emission energies.

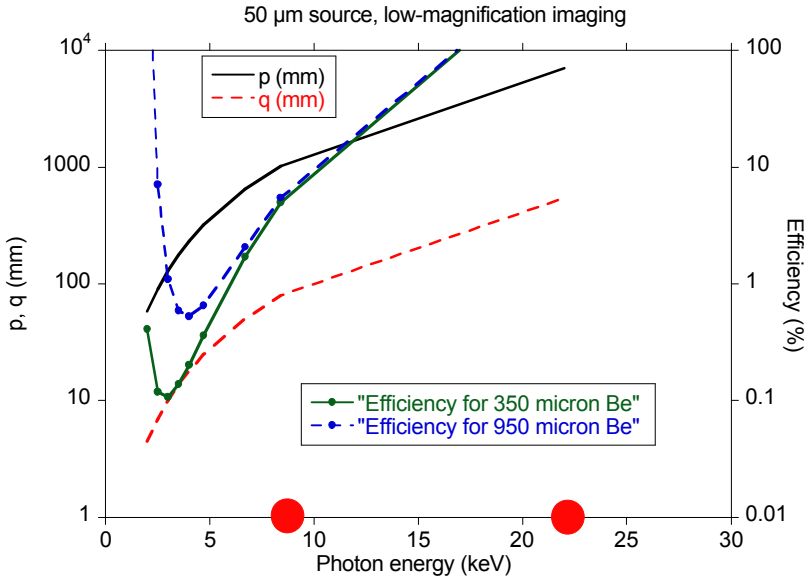

Figure 9: Required full-source imaging parameters to match Kevex resolution, contrast, and signal-to-noise, with a 50 µm source and low magnification. Required efficiencies assume a 300-J laser and 50% detection efficiency. Also plotted are experimental data points from Titan area backlight targets.

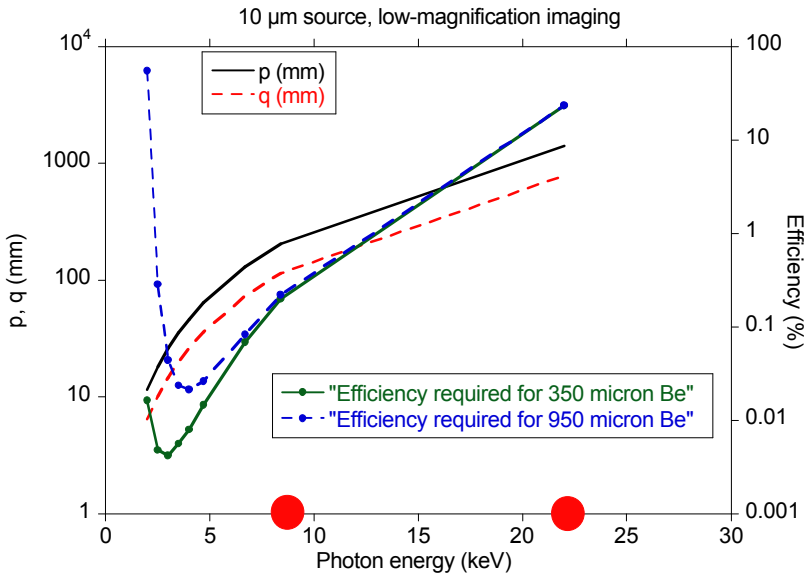

Figure 10: Required full-source imaging parameters to match Kevex resolution, contrast, and signal-to-noise, with a 10 µm source and low magnification. Required efficiencies assume a 300-J laser and 50% detection efficiency. Also plotted are experimental data points from Titan restricted source targets.

We see that there is a large gap between experimentally-measured conversion efficiencies and requirements for matching current Kevex laboratory data. This is due to the relatively low short-pulse energy conversion efficiency, which can be more than an order of magnitude less than for thermal backlights at lower energies. The conversion efficiencies at higher x-ray energies do greatly exceed those achievable for thermal backlights, but efficiency requirements at those energies rise rapidly due to smaller refraction effects. We conclude that short-pulse plasma sources currently produced at facilities such as Titan cannot meet requirements for providing high-quality phase-contrast images of cryogenic DT capsules unless conversion efficiencies can be significantly improved while maintaining small source diameters.

3) National Ignition Facility

Assuming optimized 351-nm laser-produced plasma sources at the NIF, the data of Workman *et al*. and Dewald *et al*. suggest conversion efficiencies of ~ 3% and ~ 15% might be achieved for Ti He-α and Au M-band x-rays, respectively, for laser intensities near 1e15 W/cm^2. These efficiencies might be reduced by a factor of 2 for laser intensities near 1e16 W/cm^2. A single NIF beam can be expected to provide ~ 5 kJ of 351-nm laser light on-target, with a ~ 2.5 TW/beam maximum power limit that requires a 2-ns laser pulse. In order to provide a laser intensity of 1e15 W/cm^2, the focus diameter would need to be 570 µm, while for a laser intensity of 1e16 W/cm^2, the focus diameter would need to be 180 µm. Assuming a 4 µm pinhole aperture and high-magnification imaging, we can plot the expected results against requirements.

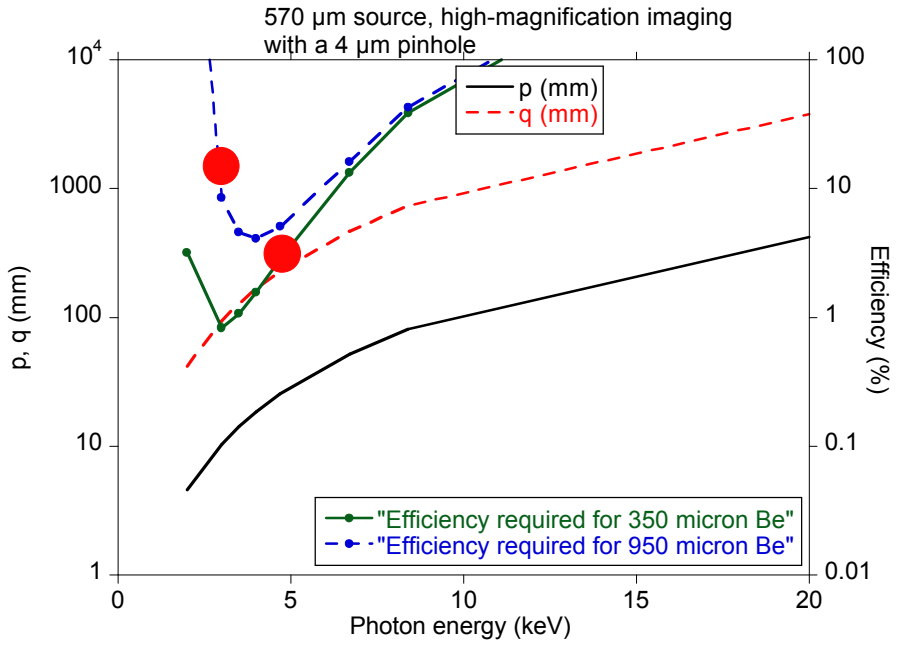

Figure 11: Required pinhole-restricted high-magnification imaging parameters to match Kevex resolution, contrast, and signal-to-noise, with a 570 µm source and a 4 µm pinhole. Required efficiencies assume a 5 kJ 2-ns laser and 50% detection efficiency. Also plotted are expected efficiencies for optimized 351-nm sources at 1e15 W/cm^2.

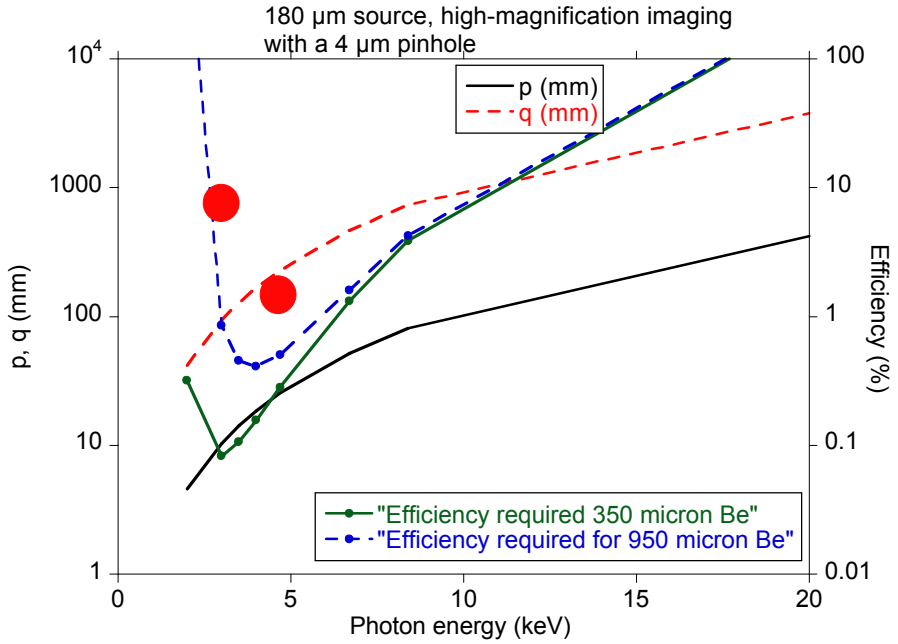

Figure 12: Required pinhole-restricted high-magnification imaging parameters to match Kevex resolution, contrast, and signal-to-noise, with a 180 µm source and a 4 µm pinhole. Required efficiencies assume a 5 kJ 2-ns laser and 50% detection efficiency. Also plotted are expected efficiencies for optimized 351-nm sources at 1e16 W/cm^2.

We find that a single NIF beam could provide high-quality pre-shot radiographs using a Au or U M-band source even with a large 570-μm defocused spot, and that the data quality would improve significantly for a tighter 180 μm-diameter focal spot. Pinhole/capsule distances are on the order of 10-20 mm, sufficient for pre-shot radiographs some nanoseconds prior to the implosion experiment; for longer time delays (for example, radiographs obtained prior to a go/no-go decision), the effects of the pinhole debris on the ignition target would need to be explored further.

V. Summary and Future Work

We have explored the requirements on source parameters and experimental geometry necessary in order to utilize laser-produced plasma x-ray sources to radiograph cryogenic DT layers in Be capsules. We find that archival data [7-11] as well as recent Janus data [13] from long-pulse laser experiments supports the prospect of using laser-produced plasmas to provide high-quality radiographs in low-magnification imaging mode. Optimal x-ray energies are in the 2-5 keV range, consistent with Au M-band, U M-band, and He-α emission from Sc or Ti. Such a geometry would require a detector with ~ 2 μm spatial resolution, and this would probably require a scintillator/microscope combination; such high-resolution detectors are available [14], but would need to be optimized for efficient detection of ~ 2-5 keV x-rays.

Backlit pinholes have been utilized in other experiments as a means to reduce the source diameter, and if this could reduce the source size to ~ 4 μm while maintaining conversion efficiency, then a high-magnification geometry could be considered instead. This would allow efficient but coarse-resolution detectors such as imaging plates to be utilized, but would exchange a short object/detector distance for a short source/object distance, possibly risking damage to the cryogenic capsule due to shrapnel and debris.

Current data from short-pulse laser facilities using foil, cone-focus wire, and buried-wire targets do not support good prospects for radiographing cryogenic DT layers in Be capsules. Short-pulse lasers are excellent for efficiently producing high-energy x-rays for radiography of dense materials, but this application works best with low-energy x-rays. In the few-keV x-ray energy region, thermal plasma sources from long-pulse lasers are more efficient. However, if good conversion efficiency in the few-keV x-ray energy range could be obtained, particularly with very small source sizes, then these lasers could become attractive.

Further experiments at Janus with smaller laser focal spots, shorter laser pulse durations, and backlit pinholes should be performed in order to determine the optimum operating point for radiography experiments at Janus. Detector development may also be required in order to produce an efficient detector with ~ 2 μm spatial resolution and sufficient dynamic range to record single-shot radiographs without saturating, but it also appears likely that a suitable detector

could be purchased commercially [14]. Finally, it appears likely that we could use a single NIF beam to obtain a pre-shot x-ray radiograph of the DT layer in-situ. This idea is attractive because it could provide data on the layer quality prior to an ignition attempt as a go/no-go decision point, or it could provide data on the layer quality essentially at ignition shot time, providing post-shot data on whether or not the layer met requirements and possibly helping to correlate ice layer asymmetries with target diagnostic data e.g. from ARC x-ray radiographs. This application would require backlit pinholes, since the NIF beam would have to irradiate a backlight target nearby, and this in turn motivates additional experiments at smaller facilities like Janus to explore and optimize backlit-pinhole x-ray sources for this application.

References

[1] Steve Haan, LLNL, Rev. 2 point design.
[2] D. N. Bittner *et al.*, Fusion Science and Technology 44, 749 (2003); B. J. Kozioziemski *et al.*, Nuclear Fusion 47, 1 (2007).
[3] B. Kozioziemski *et al.*, J. Appl. Phys. 97, 063103 (2005).
[4] O. Landen, "Refraction Enhanced Imaging from Curved Interfaces", internal memorandum, 6/14/04.
[5] Thermo Scientific model PXS927EA-LV, http://www.thermo.com/.
[6] Lawrence Berkeley Laboratory CXRO web site, http://henke.lbl.gov/optical_constants/atten2.html.
[7] D. L. Matthews *et al.*, J. Appl. Phys. 54, 4260 (1983).
[8] L. E. Ruggles *et al.*, Rev. Sci. Instrum. 74, 2206 (2003).
[9] D. W. Phillion *et al.*, Rev. Sci. Instrum. 59, 1476 (1988).
[10] J. Workman *et al.*, Proc. SPIE 4504, 168 (2001).
[11] E. Dewald *et al.*, manuscript in preparation (2007).
[12] H. -S. Park *et al.*, Phys. Plasmas 13, 056309 (2006).
[13] Nobuhiko Izumi, LLNL, personal communication.
[14] Xradia Corporation, http://xradia.com/index.html.